Supplement of Atmos. Chem. Phys., 23, 14159–14186, 2023
https://doi.org/10.5194/acp-23-14159-2023-supplement

Atmospheric Chemistry and Physics
Open Access
EGU

Supplement of

Impact of transport model resolution and a priori assumptions on inverse modeling of Swiss F-gas emissions

Ioannis Katharopoulos et al.

Correspondence to: Ioannis Katharopoulos (ioannis.katharopoulos@gmail.com) and Stephan Henne (stephan.henne@empa.ch)

S-1 Figures

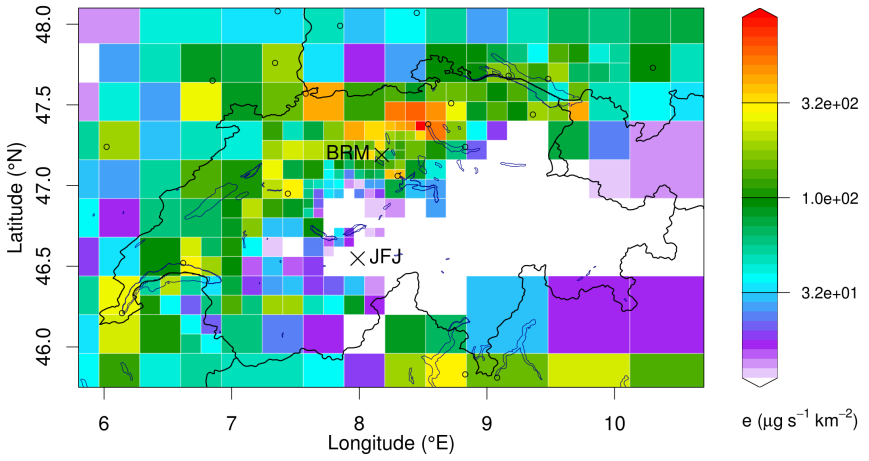

Figure S1: Spatial distribution of Swiss HFC-125 a-posteriori emissions for the base inversion (BRM and JFJ only included) for the period 2019–2020 with the 7 km model starting from a population based a-priori.

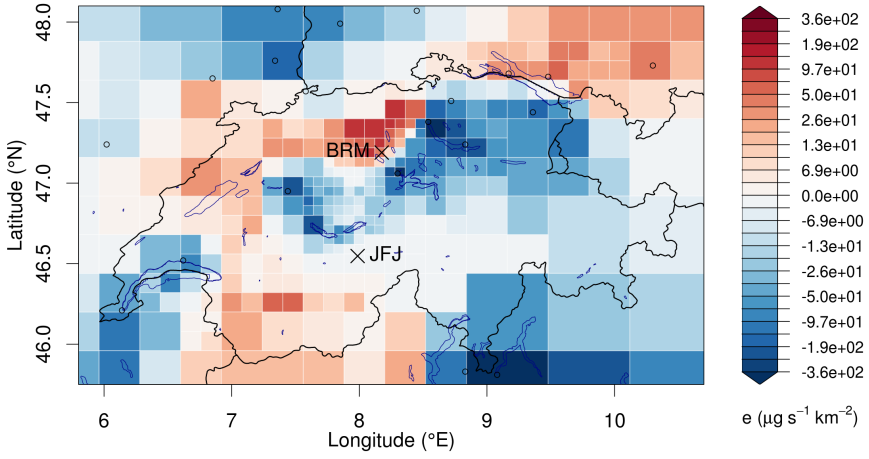

Figure S2: A-posteriori minus a-priori emission differences for HFC-125 for the base inversion with the 7 km model starting from a population based a-priori.

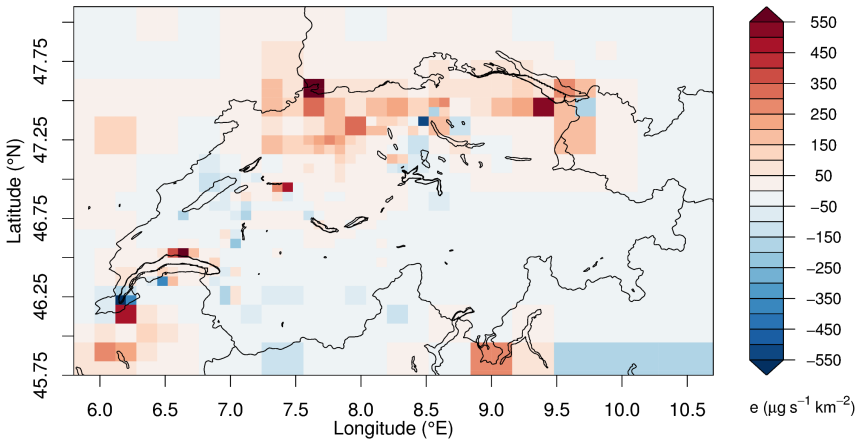

Figure S3: A-posteriori emission differences between the high- and low-resolution model inversions with population based a-priori for HFC-125

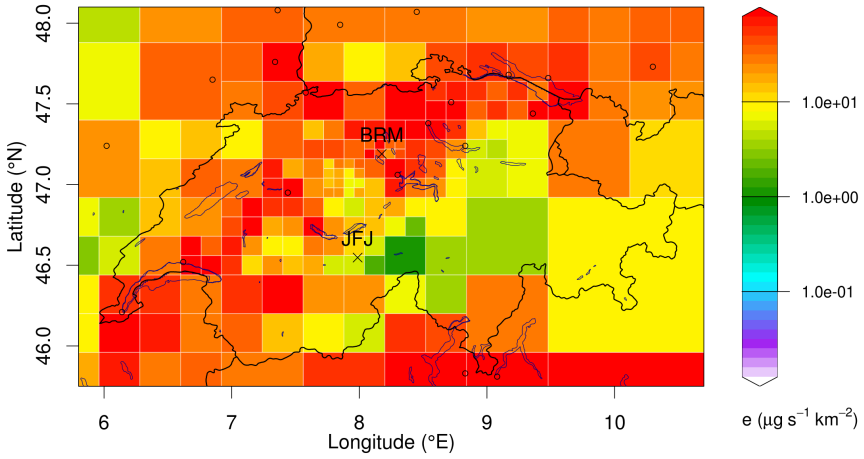

Figure S4: Spatial distribution of Swiss HFC-32 a-posteriori emissions for the base inversion (BRM and JFJ only included) for the period 2019–2020 with the 7 km model starting from a population based a-priori.

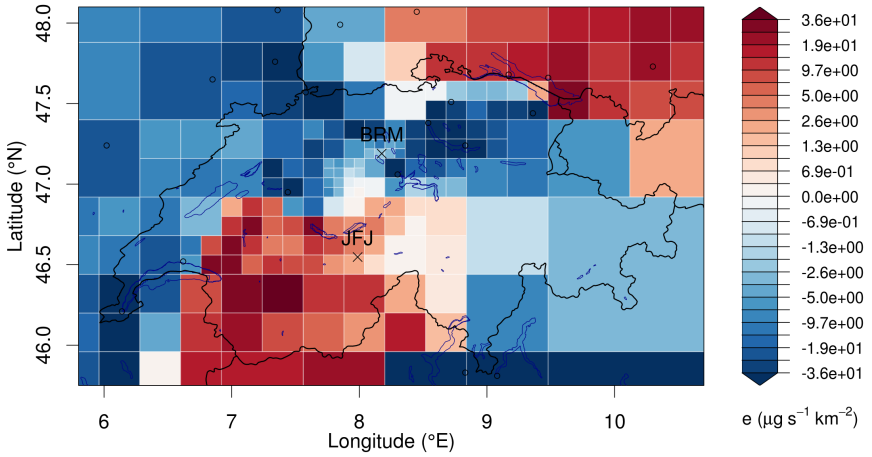

Figure S5: A-posteriori minus a-priori emission differences for HFC-125 for the base inversion with the 7 km model starting from a population based a-priori.

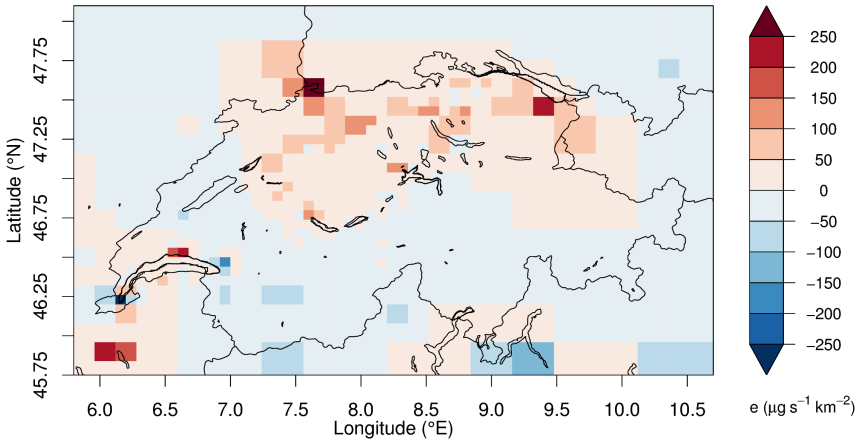

Figure S6: A-posteriori emission differences between the high- and low-resolution model inversions with population based a-priori for HFC-125

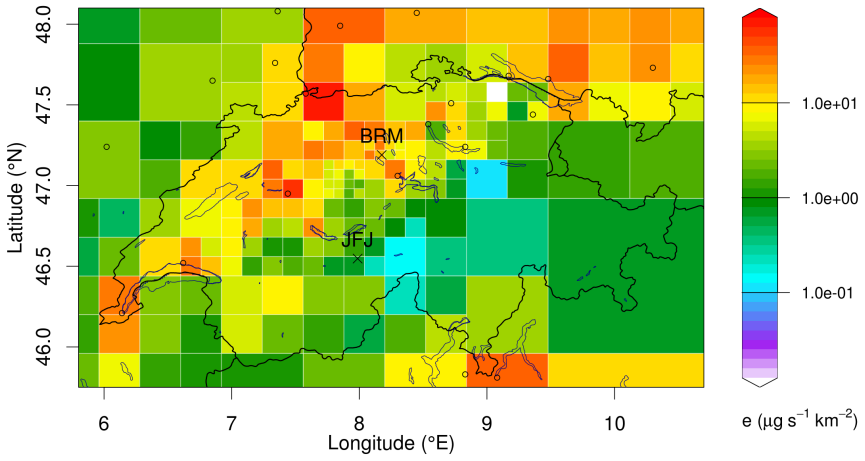

Figure S7: Spatial distribution of Swiss HFC-125 a-posteriori emissions for the base inversion (BRM and JFJ only included) for the period 2019–2020 with the 7 km model starting from a population based a-priori.

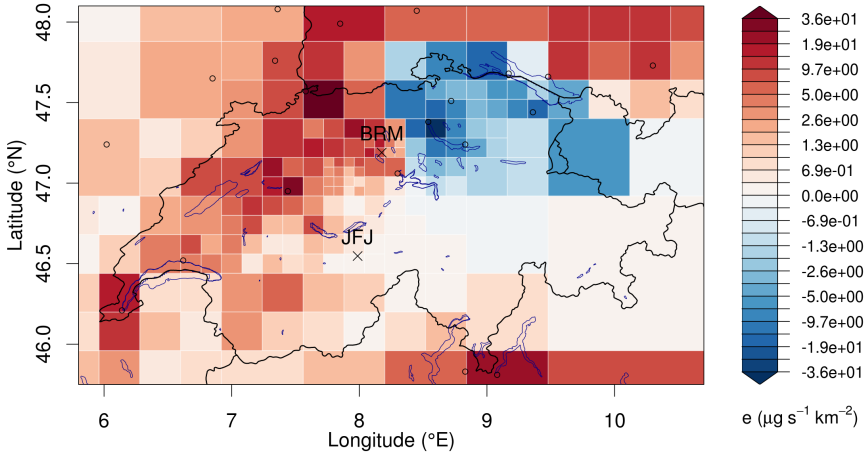

Figure S8: A-posteriori minus a-priori emission differences for HFC-125 for the base inversion with the 7 km model starting from a population based a-priori.

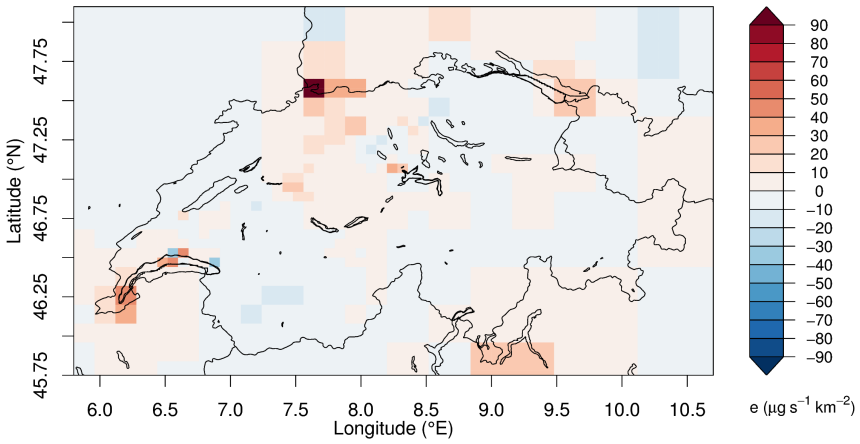

Figure S9: A-posteriori emission differences between the high- and low-resolution model inversions with population based a-priori for HFC-125

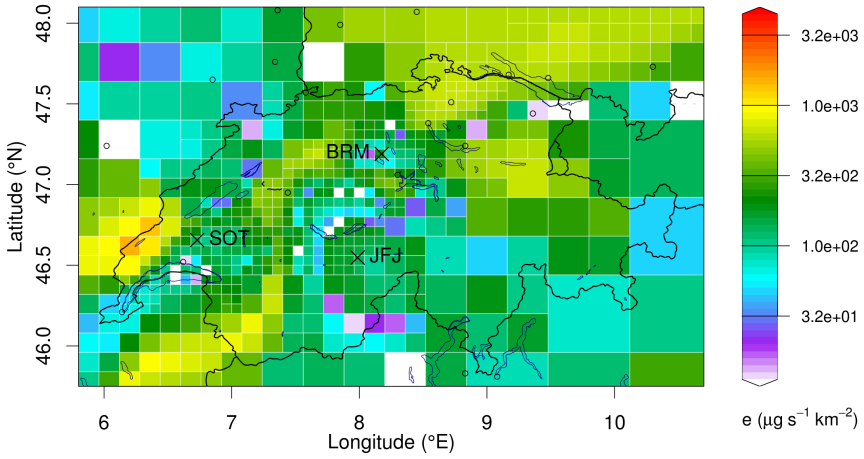

Figure S10: Spatial distribution of Swiss HFC-134a a-posteriori emissions for the inversion including both BRM and SOTT for the period 2019–2021 with the 7 km model starting from a uniform a-priori.

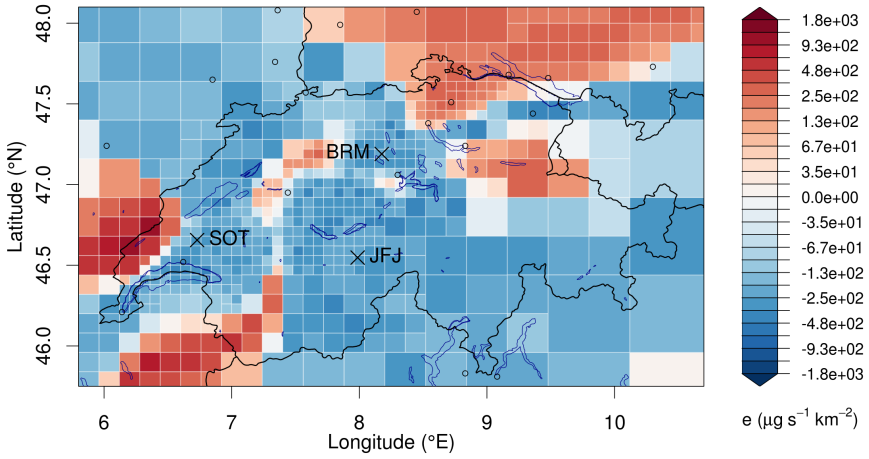

Figure S11: A-posteriori minus a-priori emission differences for HFC-134a for the inversion including both BRM and SOTT for the period 2019–2021 with the 7 km model starting from a uniform a-priori.

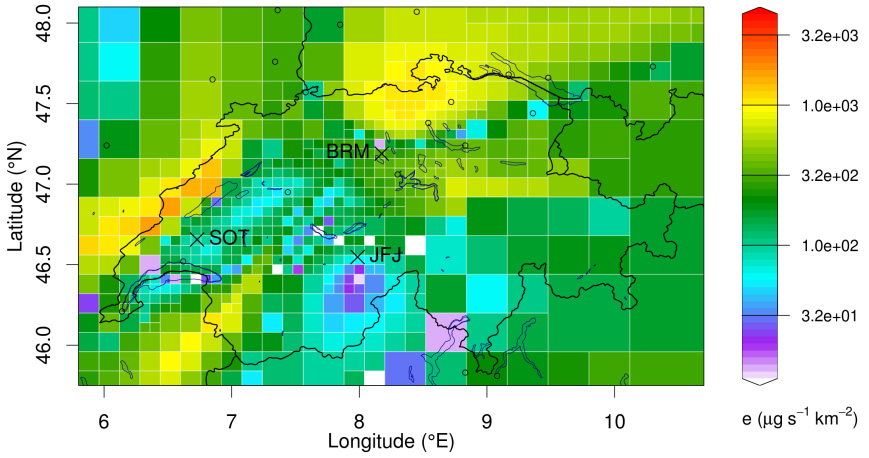

Figure S12: Spatial distribution of Swiss HFC-134a a-posteriori emissions for the inversion including both BRM and SOTT for the period 2019–2021 with the 1 km model starting from a uniform a-priori.

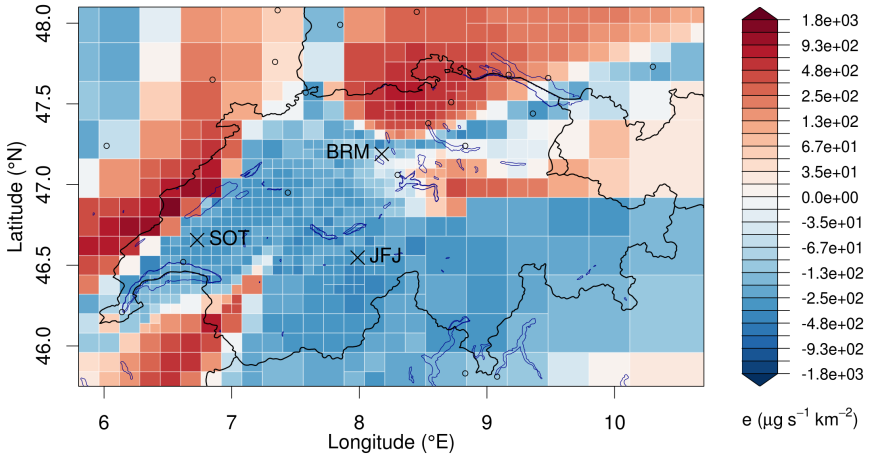

Figure S13: A-posteriori minus a-priori emission differences for HFC-134a for the inversion including both BRM and SOTT for the period 2019–2021 with the 1 km model starting from a uniform a-priori.

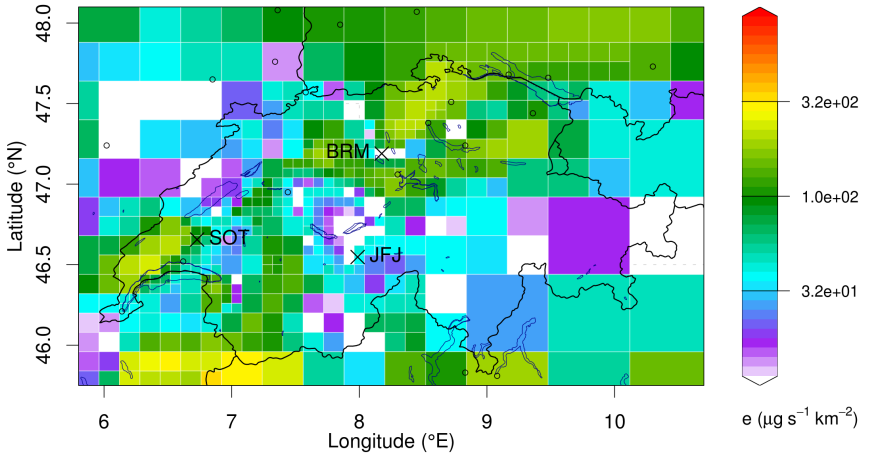

Figure S14: Spatial distribution of Swiss HFC-125 a-posteriori emissions for the inversion including both BRM and SOTT for the period 2019–2021 with the 7 km model starting from a uniform a-priori.

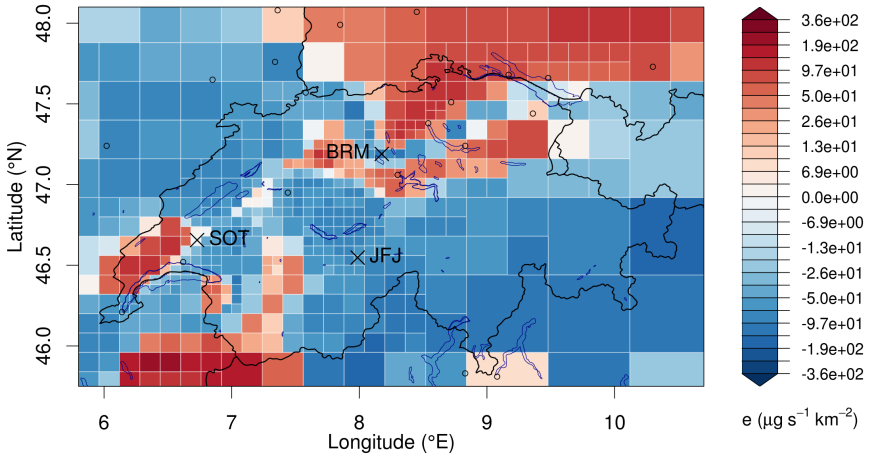

Figure S15: A-posteriori minus a-priori emission differences for HFC-125 for the inversion including both BRM and SOTT for the period 2019–2021 with the 7 km model starting from a uniform a-priori.

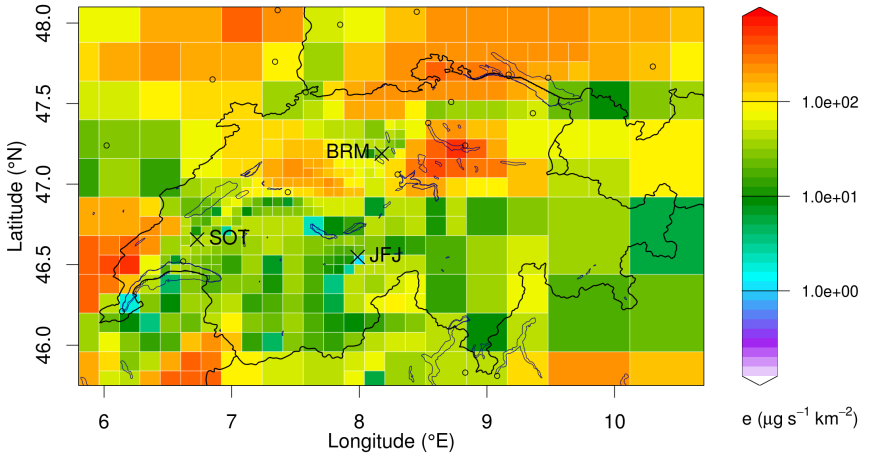

Figure S16: Spatial distribution of Swiss HFC-125 a-posteriori emissions for the inversion including both BRM and SOTT for the period 2019–2021 with the 1 km model starting from a uniform a-priori.

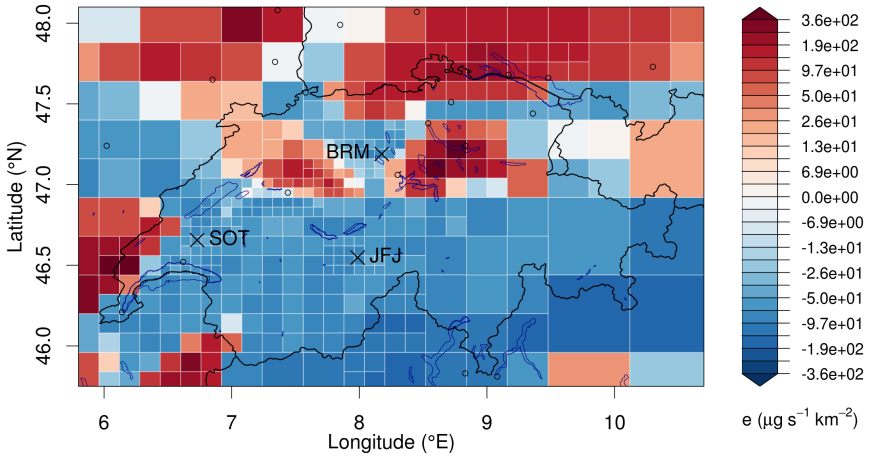

Figure S17: A-posteriori minus a-priori emission differences for HFC-125 for the inversion including both BRM and SOTT for the period 2019–2021 with the 1 km model starting from a uniform a-priori.

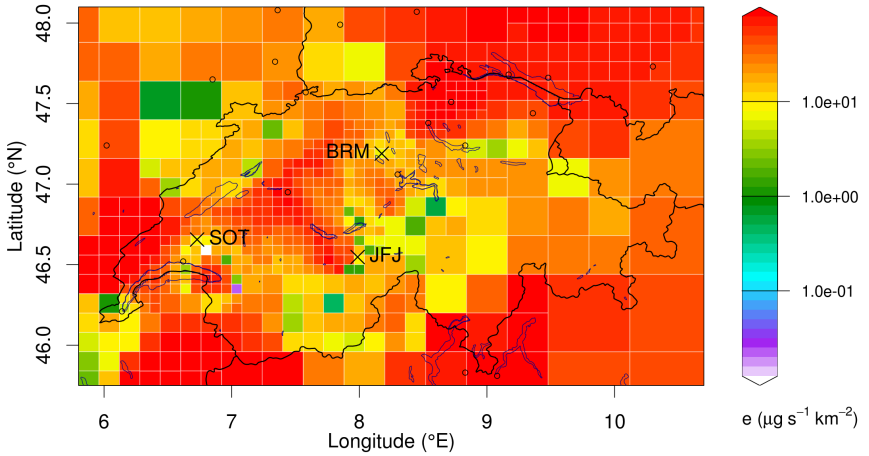

Figure S18: Spatial distribution of Swiss HFC-32 a-posteriori emissions for the inversion including both BRM and SOTT for the period 2019–2021 with the 7 km model starting from a uniform a-priori.

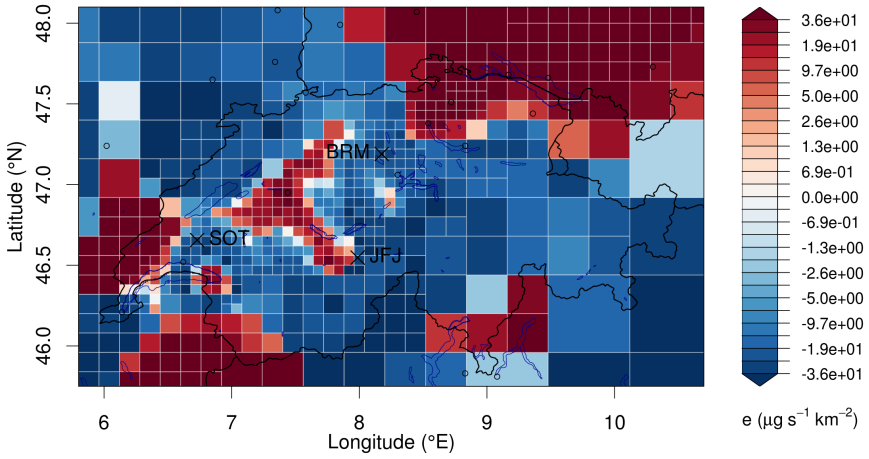

Figure S19: A-posteriori minus a-priori emission differences for HFC-32 for the inversion including both BRM and SOTT for the period 2019–2021 with the 7 km model starting from a uniform a-priori.

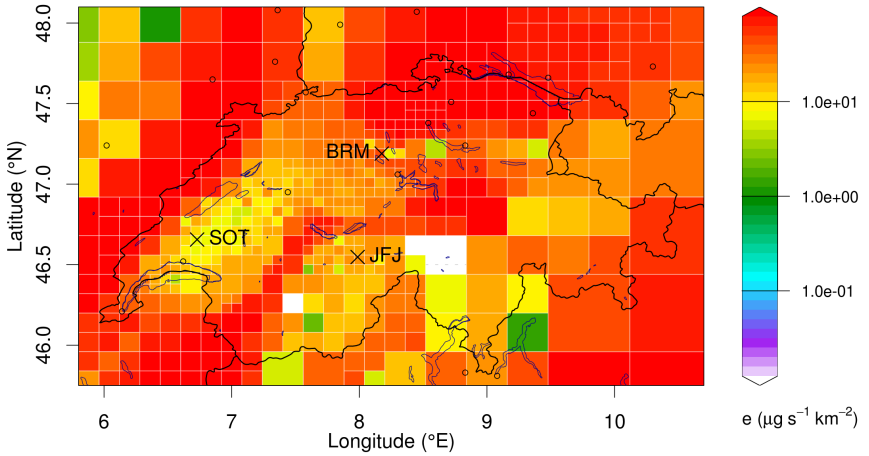

Figure S20: Spatial distribution of Swiss HFC-32 a-posteriori emissions for the inversion including both BRM and SOTT for the period 2019–2021 with the 1 km model starting from a uniform a-priori.

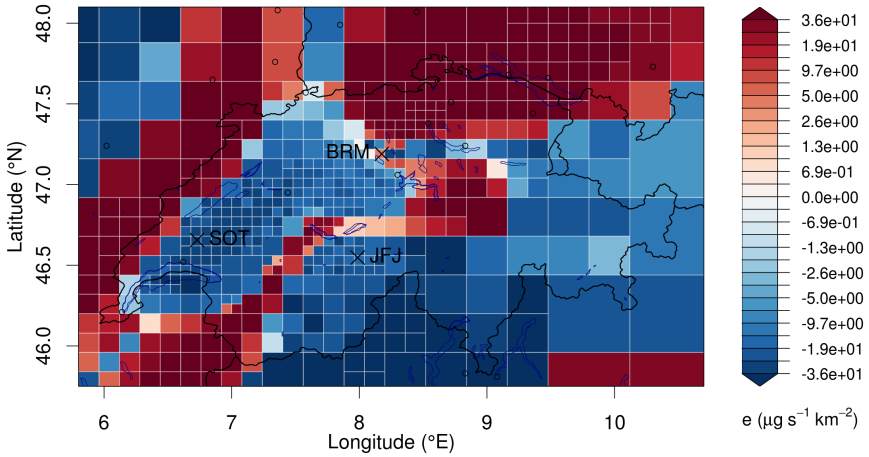

Figure S21: A-posteriori minus a-priori emission differences for HFC-32 for the inversion including both BRM and SOTT for the period 2019–2021 with the 1 km model starting from a uniform a-priori.

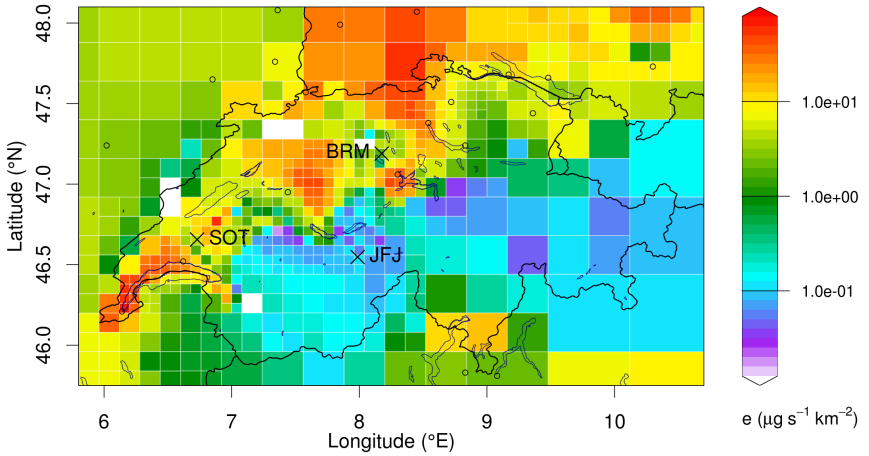

Figure S22: Spatial distribution of Swiss SF_6 a-posteriori emissions for the inversion including both BRM and SOTT for the period 2019–2021 with the 7 km model starting from a uniform a-priori.

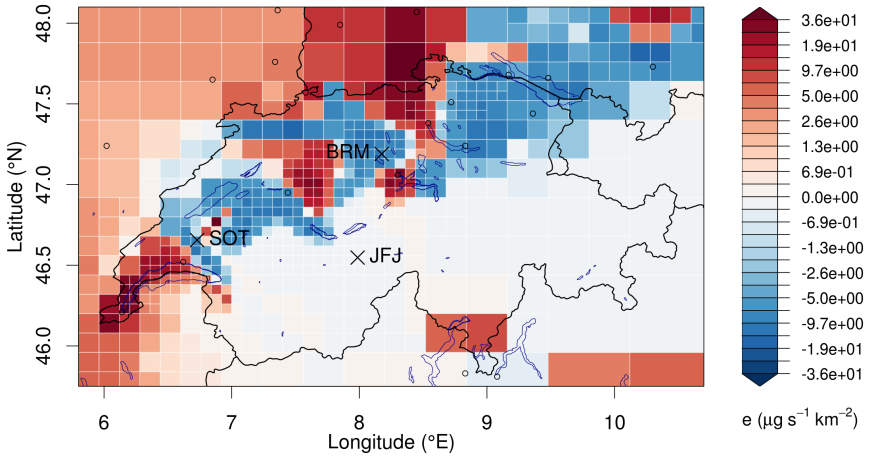

Figure S23: A-posteriori minus a-priori emission differences for SF_6 for the inversion including both BRM and SOTT for the period 2019–2021 with the 7 km model starting from a uniform a-priori.

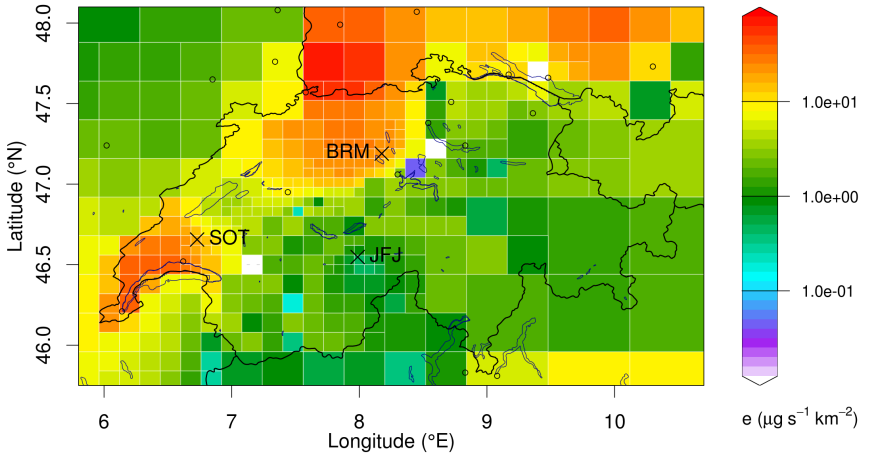

Figure S24: Spatial distribution of Swiss SF_6 a-posteriori emissions for the inversion including both BRM and SOTT for the period 2019–2021 with the 1 km model starting from a uniform a-priori.

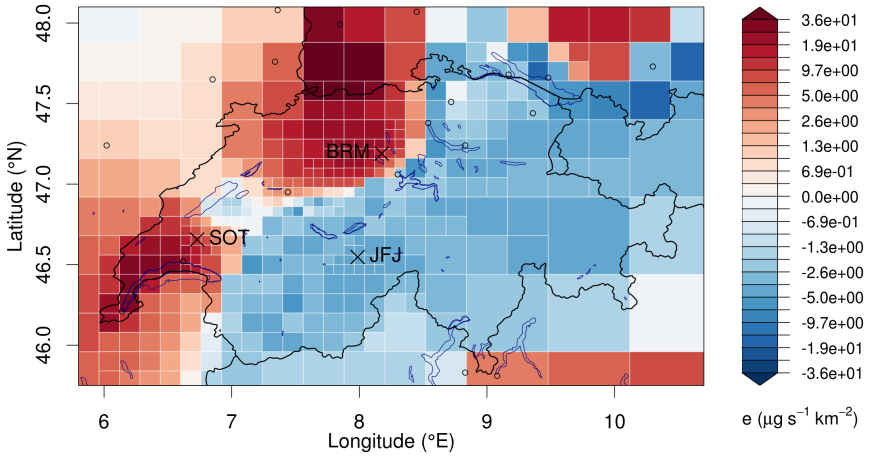

Figure S25: A-posteriori minus a-priori emission differences for SF_6 for the inversion including both BRM and SOTT for the period 2019–2021 with the 1 km model starting from a uniform a-priori.

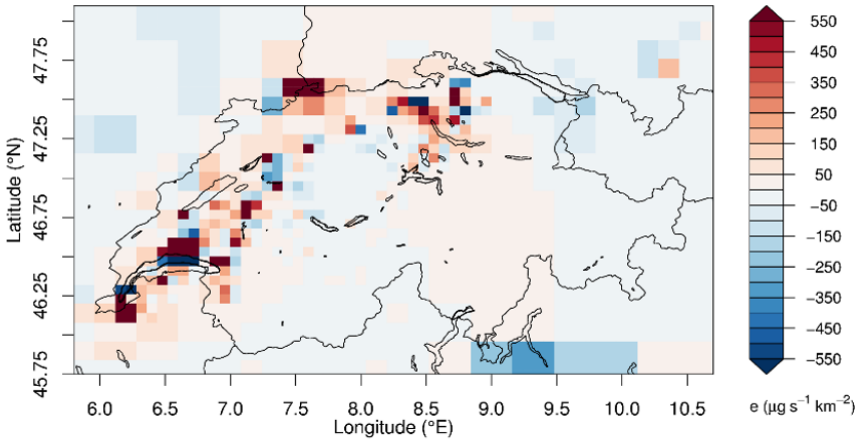

Figure S26: A-posteriori emission differences between the high- model inversions with and without SOTT for a population based a-priori for HFC-134a.

Table S1: Statistical measures used to assess the a-priori performance of the transport model for different compounds, different model resolutions, and different a-priori emission distributions. The table displays root means squared error (RMSE), and correlations of simulated compound values against observations for Beromünster (BRM) and Sottens (SOT)

Compound	Model Res.	A-priori	r (BRM)	r (SOT)	RMSE (BRM) (ppt)	RMSE (SOT) (ppt)
HFC-134a	C7	Population	0.70	0.65	9.33	9.10
HFC-134a	C7	Uniform	0.66	0.67	6.01	5.78
HFC-134a	C7	Elevation-dep	0.64	0.57	9.45	10.3
HFC-134a	C1	Population	0.78	0.81	6.33	6.20
HFC-134a	C1	Uniform	0.73	0.76	4.84	4.92
HFC-134a	C1	Elevation-dep	0.75	0.74	6.53	7.60
HFC-125	C7	Population	0.69	0.63	1.62	1.94
HFC-125	C7	Uniform	0.61	0.67	1.42	1.38
HFC-125	C7	Elevation-dep	0.62	0.52	1.64	2.16
HFC-125	C1	Population	0.69	0.80	1.30	1.34
HFC-125	C1	Uniform	0.60	0.77	1.42	1.19
HFC-125	C1	Elevation-dep	0.66	0.72	1.30	1.58
HFC-32	C7	Population	0.61	0.59	1.98	2.16
HFC-32	C7	Uniform	0.61	0.62	1.66	2.08
HFC-32	C7	Elevation-dep	0.56	0.50	1.98	2.30
HFC-32	C1	Population	0.68	0.77	1.55	1.67
HFC-32	C1	Uniform	0.65	0.74	1.61	1.93
HFC-32	C1	Elevation-dep	0.64	0.70	1.60	1.84
SF_6	C7	Population	0.51	0.41	0.183	0.293
SF_6	C7	Uniform	0.50	0.37	0.189	0.312
SF_6	C7	Elevation-dep	0.50	0.37	0.181	0.298
SF_6	C1	Population	0.60	0.49	0.173	0.290
SF_6	C1	Uniform	0.58	0.43	0.188	0.310
SF_6	C1	Elevation-dep	0.59	0.42	0.173	0.294

Table S2: Statistical measures used to assess the reliability of inversion for different compounds, different transport model resolutions, different a-priori emissions, and for inversions with seasonal emissions. The table displays the reduced χ^2 index, degrees of freedom (DOF), root means squared error (RMSE), and correlations of simulated compound values against observations for Beromünster (BRM) and Sottens (SOT).

Compound	Model Res.	Sensitivity	χ^2	DOF	r (BRM)	r (SOT)	RMSE (BRM) (ppt)	RMSE (SOT) (ppt)
HFC-134a	C7	SEAS1	0.89	252	0.78	0.81	4.2	4.3
HFC-134a	C7	SEAS2	1.40	329	0.73	0.76	4.7	4.8
HFC-134a	C1	SEAS1	0.90	199	0.85	0.85	3.5	3.9
HFC-134a	C1	SEAS2	1.30	303	0.81	0.81	3.9	4.4